THE JOURNAL OF PHYSICAL CHEMISTRY C

Article

pubs.acs.org/JPCC

Influence of Film and Substrate Structure on Photoelectron Momentum Maps of Coronene Thin Films on Ag(111)

Christian Udhardt,[†] Felix Otto,[†] Christian Kern,[‡] Daniel Lüftner,[‡] Tobias Huempfner,[†] Tino Kirchhuebel,[†] Falko Sojka,[†] Matthias Meissner,[†,§] Bernd Schröter,[†] Roman Forker,[†] Peter Puschnig,*[,‡] and Torsten Fritz*[,†]

[†]Institute of Solid State Physics, Friedrich Schiller University Jena, Helmholtzweg 5, 07743 Jena, Germany

[‡]Institute of Physics, University of Graz, NAWI-Graz, Universitätsplatz 5, 8010 Graz, Austria

ABSTRACT: Angle-resolved ultraviolet photoelectron spectroscopy (ARUPS) was measured for one-monolayer coronene films deposited on Ag(111). The (k_x,k_y)-dependent photoelectron momentum maps (PMMs), which were extracted from the ARUPS data by cuts at fixed binding energies, show finely structured patterns for the highest and the second-highest occupied molecular orbitals. While the substructure of the PMM main features is related to the 4 × 4 commensurate film structure, various features with three-fold symmetry imply an additional influence of the substrate. PMM simulations on the basis of both free-standing coronene assemblies and coronene monolayers on the Ag(111) substrate confirm a sizable molecule−molecule interaction because no substructure was observed for PMM simulations using free coronene molecules.

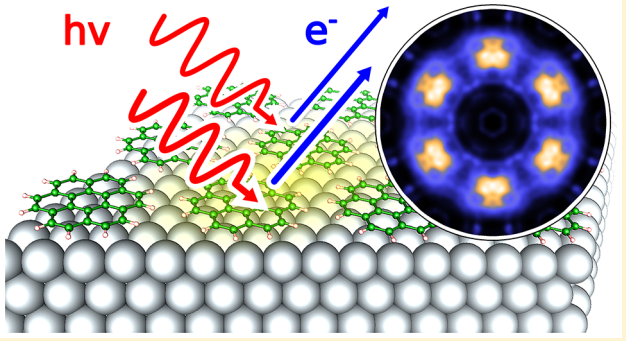

INTRODUCTION

As has been shown for a number of well-ordered organic adsorbates on crystalline surfaces, the photoelectron angular distributions of adsorbate-derived molecular states, also termed photoelectron momentum maps (PMMs), can be essentially described by a Fourier transform of the molecular orbitals computed for the free molecule.[1−5] By additionally considering band structure and Bloch states, substructures of the main PMM features can also be explained with high precision.[6] Recent angle-resolved ultraviolet photoelectron spectroscopy (ARUPS) measurements of one monolayer (1 ML) coronene thin films on Au(111) demonstrated that the momentum maps are further influenced by vibrational modes, dispersion of the molecular states, and back-folded substrate bands.[7] Single scattering cluster/molecular orbital (SSC/MO) and independent atomic center/molecular orbital (IAC/MO) calculations[8] have shown that additional fine features in the momentum maps can be described by scattering events at the second-nearest-neighbor approximation.

Recently, potassium-intercalated coronene has attracted attention for showing superconducting properties with transition temperatures up to 15 K.[9] In contrast with the samples investigated here (epitaxially grown molecular layers on a single-crystalline substrate), the samples of ref 9 were powder samples prepared by annealing nominal compositions of dopant and organic compound. In the case of epitaxially grown films, effects of charge transfer, that is, doping of the molecular layer, can also be caused by the interaction with the substrate.[10]

Here, we present electronic and structural details of 1 ML coronene thin films deposited on Ag(111). In particular, we discuss the substructures in the PMMs of the highest (HOMO) and the second-highest occupied molecular orbital (HOMO−1) in relation to the adsorbate film structure[11,12] and the three-fold symmetry of the substrate surface. Considering the phase alignment and the degeneracy of the orbitals, the influence of the molecular aggregation on the PMM of the HOMO will be shown by means of simulations. A further aim of this study is to clarify the molecular orientation of coronene molecules in monolayers by structural optimizations using density functional theory (DFT).

METHODOLOGY

Experimental Details. All experiments were performed in ultrahigh vacuum (UHV) chambers with a base pressure in the 10^{-10} mbar range.

The Ag(111) and Au(111) substrates were prepared by several sputtering and annealing cycles according to standard procedures.[13] Coronene (obtained from Sigma-Aldrich and then purified via temperature gradient sublimation) was deposited onto the substrates held at room temperature using a temperature-stabilized effusion cell heated to about 100−110 °C.[11]

A surface analysis system (SPECS Surface Nano Analysis GmbH) was used for the photoemission experiments. The light

Received: April 13, 2017
Published: May 11, 2017

DOI: 10.1021/acs.jpcc.7b03500
J. Phys. Chem. C 2017, 121, 12285−12293

source (aligned for He(I)α excitation and p-polarization) was a microwave-heated gas discharge lamp (UVLS) in combination with a toroidal-mirror monochromator (TMM 304), where the angle of incidence with respect to the direction of the electron detection was 50°. We measured the photoemission rate with a hemispherical electron energy analyzer (PHOIBOS 150), which was equipped with a delay line detector (3D-DLD4040-150) operated at different measurement modes. While the 2D mode of the detector takes images (300 × 200 channels) with a fixed kinetic energy (17 to 22 eV) and a fixed angular range (−13.5 to +13.5°, of which only −7 to +9° was used), the 1D mode (angular resolution was set to ±1° by using the entrance slit of the detector) acquired an integrated detector signal as spectrum. For the UPS measurements, the sample was mounted on a five-axis manipulator (x, y, z, polar angle θ, and azimuthal angle ϕ) cooled with liquid helium ($T_{sample} \lesssim 30$ K). During the measurements (several hours) no beam damage could be detected.

The PMMs were obtained by measuring ARUPS in the 2D mode, integrating the single images in a range from −0.125 eV to +0.125 eV around a given binding energy E_b. Measurements were taken every 15° azimuthal angle (ranging from −60° to +60°) as well as every 2° polar angle, where symmetry considerations were applied subsequently by rotating the data by 120 and 240° azimuthally. In contrast, the ARUPS data, the polar scans (PS), and the azimuthal scans (AS) were acquired in the 1D mode in angular steps of 2°. While the UPS spectra, the ARUPS data, and the angular scans were smoothed with Savitzky Golay filters, the momentum maps were smoothed with a Gaussian filter, adding a high-pass filter afterward to increase the visibility of low-intensity features. The intensity curves of the angular scans were obtained by integrating the peaks after subtracting a linear background. In the case of the HOMO, the integration range was 1.9 to 3.2 eV binding energy, while that of the HOMO−1 was 3.5 to 3.9 eV. Measurement parameters (θ, ϕ, and the nonenergy channel ϑ of the detector) were converted into momentum space (k_x and k_y) using the standard equations from the literature.[14,15] All data were furthermore divided by cos(θ) to account for the electron emission characteristic.

To elucidate the molecular orientation in the adsorbate film with high precision, scanning tunneling microscopy (STM) was performed at ∼1.1 K with a JT-STM (SPECS Surface Nano Analysis GmbH). The details of the device are published elsewhere.[11,16]

Computational Details. Two types of ab initio electronic structure calculations were performed within the framework of DFT. First, DFT calculations for gas-phase coronene molecules were performed with Gaussian 09 using the hybrid-functional B3LYP and the 6-311++G(d,p) basis set.[17] We then simulated the momentum maps by calculating the ARUPS intensity $I(k_x, k_y)$ with the algorithm published in ref 1. In our experimental setup, the angle-dependent factor $|\vec{A} \cdot \vec{k}|$, which appears in the formula of $I(k_x,k_y)$ (derived from Fermi's Golden Rule), is in good approximation a constant and was thus neglected in the simulations.

Second, DFT electronic structure calculations for a coronene monolayer arranged in the 4 × 4 overlayer structure adsorbed on Ag(111) and Au(111) have been carried out using a repeated-slab approach utilizing the Vienna Ab initio Simulation Package (VASP).[18−20] The metallic substrate has been modeled by five metallic layers adding a vacuum layer of ∼18 Å between the slabs. To avoid spurious electric fields, a dipole layer was furthermore inserted in the vacuum region.[21] The generalized gradient approximation (GGA)[22] and the projector augmented wave (PAW) approach[23] were used for exchange-correlation effects and allowing for a relatively low kinetic energy cutoff of ∼500 eV, respectively. For the geometric relaxation we used a Monkhorst−Pack[24] 4 × 4 × 1 grid of k-points, and a 6 × 6 × 3 grid was used for the electronic structure calculations, combined with a first-order Methfessel−Paxton smearing of 0.1 eV.[25] During the geometry optimization, the atomic positions of the molecular layer and the first two metallic layers were allowed to relax. To account for van der Waals interactions, which are ill-described in standard GGA functionals,[26,27] we employed the vdW-surf method according to Ruiz et al.[28,29] during the geometry optimization. No symmetry restrictions were applied. The simulation of PMMs within the final-state plane-wave approximation followed the advanced approach described in refs 6 and 30.

RESULTS

Structural Properties. Before focusing on the electronic properties, we discuss the geometric structure of coronene monolayer films deposited on Ag(111) and on Au(111) by means of STM images and DFT structural optimizations. Previous STM and low-energy electron diffraction (LEED) measurements on coronene films on Ag(111) revealed that submonolayer films are poorly ordered up to a coverage of 0.9 ML.[11] The molecules adopt a noncommensurate film structure for increasing coverage, which continuously changes to a 4 × 4 commensurate superstructure at the coverage of 1 ML. In the case of coronene monolayers on Au(111), the films adopt a 4 × 4 geometry as well, as shown in ref 31 by means of LEED and STM.

The hexagonal overlayer periodicity can be clearly recognized in the STM images of 1 ML coronene films on Ag(111) and on Au(111) shown in Figure 1a,b. Because the molecular features appear more smeared out in the case of Ag(111), we choose Au(111) as reference for an analysis of the azimuthal

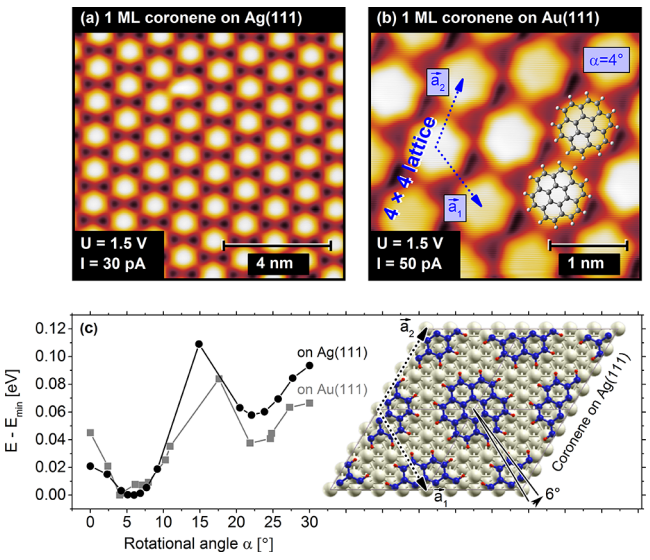

Figure 1. STM images of 1 ML coronene films on (a) Ag(111) and (b) Au(111). (c) Optimization of the molecular rotation on both surfaces. The inset of panel c shows the optimized geometry of the 4 × 4 coronene slab on Ag(111).

DOI: 10.1021/acs.jpcc.7b03500
J. Phys. Chem. C 2017, 121, 12285−12293

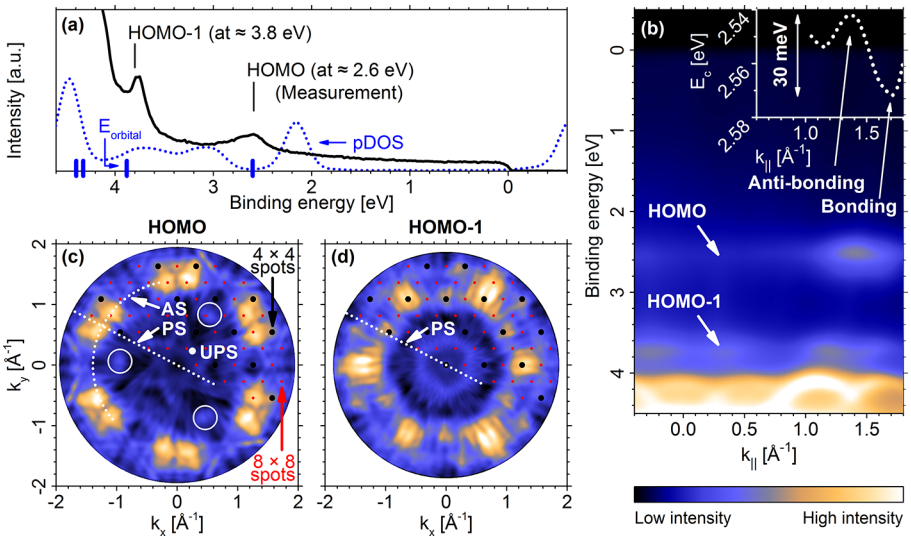

Figure 2. (a) UPS spectrum and (b) ARUPS diagram of a 1 ML coronene film deposited on Ag(111). Energy positions of a free coronene molecule and the pDOS of a coronene monolayer on Ag(111) obtained from DFT are shown in panel a as vertical blue marks and as a blue dotted line, respectively. The inset in panel b depicts the center energy of the HOMO feature as a function of $k_{\parallel}$. (c,d) Photoelectron momentum maps of the HOMO and the HOMO−1. The measurement position of the UPS data in panel a is depicted in panel c by a white point. White dotted lines in panels c and d indicate the directions of the azimuthal scans (ASs) and the polar scans (PSs), evaluated in detail in Figure 4. The measurement direction of the ARUPS data in panel b is the same as that for the PS.

orientation of coronene, which we define as the angle between the zigzag direction of the molecule and the substrate's $[10\bar{1}]$ direction ($\vec{a}_1$). The STM image on Au(111) suggests that the molecules are rotated noticeably against the adsorbate lattice vectors because neither the tips nor the edges of the bright hexagons representing the coronene molecules are facing each other. In the case of the 4 × 4 structure, azimuthal angles of ∼7° or ∼23° with respect to $\vec{a}_1$ are plausible due to the repulsion of the H atoms, leading to an interdigitated alignment of the coronene molecules within the unit cell. Indeed, the structural optimization of the 4 × 4 coronene monolayer on the Au(111) surface, which was performed by calculating the total energy with DFT ($E - E_{min}$) at various azimuthal orientations, resulted in an overall minimum at ∼4° (Figure 1c). In accordance with the DFT optimization, two molecules being rotated by the energetically favored configuration (4°) are overlaid to the STM image on Au(111) (Figure 1b), thereby confirming the molecular rotation as appearing in the STM image. The small deviation to the experimental value (∼7°) could be due to the Au(111) surface reconstruction,[32] which was not considered in the DFT calculations. Because the unit-cell dimensions are identical on the Au(111) and the Ag(111) surface,[11,31] a similar film geometry is expected in both cases, although a Ag(111) surface reconstruction is not present. In the case of Ag(111), the calculation of the total energy shows that the energetically favored configuration adopts a rotational angle of 6°, which is, as expected, close to the rotational angle on Au(111).

It should be noted that previous investigations of coronene films on Ag(111) report, in addition to an azimuthal rotation, an out-of-plane tilt of the molecules as deduced from STM and force-field calculations[12] as well as by near-edge X-ray absorption fine structure (NEXAFS) measurements.[33] In the case of the NEXAFS measurements, however, 2 to 3 ML thick films had been prepared, where a tilt of the molecules in the second and higher layers might be responsible for the overall molecular tilt concluded.[33] In contrast to the NEXAFS measurement on Ag(111), carbon K-edge XAFS measured on coronene monolayers on Au(111) confirmed flat-lying molecules.[31] We emphasize that our DFT structural optimizations do not indicate an out-of-plane tilt of the molecules on either the Ag(111) or on the Au(111) surface. Even when started from a tilted configuration, the molecules relaxed into a film geometry with flat-lying molecules.

Electronic Structure. After focusing on the structural details, we move on to the electronic structure of the coronene/Ag(111) interface. Figure 2a shows an experimental UPS spectrum as well as the Kohn−Sham orbital energies of a free molecule (vertical blue marks) and the projected density of states (pDOS) of a 4 × 4 coronene monolayer on Ag(111) from the DFT calculation (blue dotted line). A work function of 3.8 eV was determined from a further UPS measurement taking into account the low kinetic energy cutoff, which can be compared with a value of 3.6 eV from the DFT calculations. The comparison between experiment and theory suggests to assign the peak at 2.6 eV to the HOMO and the one at 3.8 eV to the HOMO−1. Note that the computed gas-phase energy levels have been aligned with the experimental HOMO energy position.

As can be seen from the ARUPS diagram (Figure 2b), both the HOMO as well as the HOMO−1 have an intensity variation depending on $k_{\parallel}$. Below 4 eV binding energy, a two-times back-folded substrate band appears in the ARUPS diagram with a k-point distance of 0.6 Å^{-1} between the band maxima. A dispersion of ∼30 meV for the HOMO band, which was elucidated by plotting the center position of the peak against $k_{\parallel}$ (Figure 2b, inset), suggests an intermolecular electronic coupling of the HOMOs, upon which a HOMO-derived band is formed. A dispersion of 30 meV was measured in the case of the azimuthal scan as well (cf. Figure 4a).

Panels c and d of Figure 2 present constant binding energy momentum maps at the energies of the HOMO and the HOMO−1, respectively. In the case of the HOMO (Figure 2c), the momentum map shows six broad maxima, which are

DOI: 10.1021/acs.jpcc.7b03500
J. Phys. Chem. C 2017, 121, 12285−12293

located in the outer region of the map. Similarly, also the momentum map of the HOMO−1 (Figure 2d) is characterized by six strong maxima that are, however, rotated by 30° compared with the features in the HOMO map.

While the overall appearance of the maps can be related to simulations of single molecules (see the subsequent section), there exists a number of substructures that cannot be explained in such a simple manner. The inner star-like structure observed in the HOMO PMM is, for example, similar to that observed for the Fermi surface of 1 ML coronene on Au(111)[7] as well as to that observed for the Fermi surface of Ca-intercalated graphene[34] and can be explained by a back-folding of substrate bands. The three-fold symmetry of the Ag(111) substrate further becomes visible as small intensity maxima in the inner area (highlighted by white circles in Figure 2c), for which no analogue can be found at ±60° azimuthal rotation. Because the main maxima are not equally intense, the three-fold symmetry of the substrate is also apparent for the HOMO−1. The reciprocal lattice spots of an 8 × 8 and a 4 × 4 superstructure (which were independently calculated from the adsorbate lattice) are superimposed on the momentum maps and qualitatively explain the substructure of the main features with good precision. It is the objective of the remaining sections to explain the features and the substructure observed in the PMMs starting from free coronene molecules through free-standing assemblies of molecules to the DFT description of the coronene/Ag(111)-interface.

Momentum Maps of Single Molecules. As a first step, momentum map simulations based on the free coronene molecule are revisited.[35] Figure 3a,b shows z-integrated probability maps (numerical summation of $|\Psi|^2(x, y, z)$ in the z-direction) as real-space representations of the HOMO and the HOMO−1. The corresponding simulated momentum maps are shown below (Figure 3c,d). Note that the kinetic energy values for the HOMO and the HOMO−1 simulations were taken from the UPS measurement (Figure 2a) and are 14.8 and 13.6 eV, respectively. Because the HOMO and the HOMO−1 are doubly degenerate,[36] the simulations were performed separately, superimposing the results afterward. The simulated PMMs (Figure 3c,d) are in accordance with those of ref 35 and explain the main features of our measurements (Figure 2c,d), albeit without the substructure.

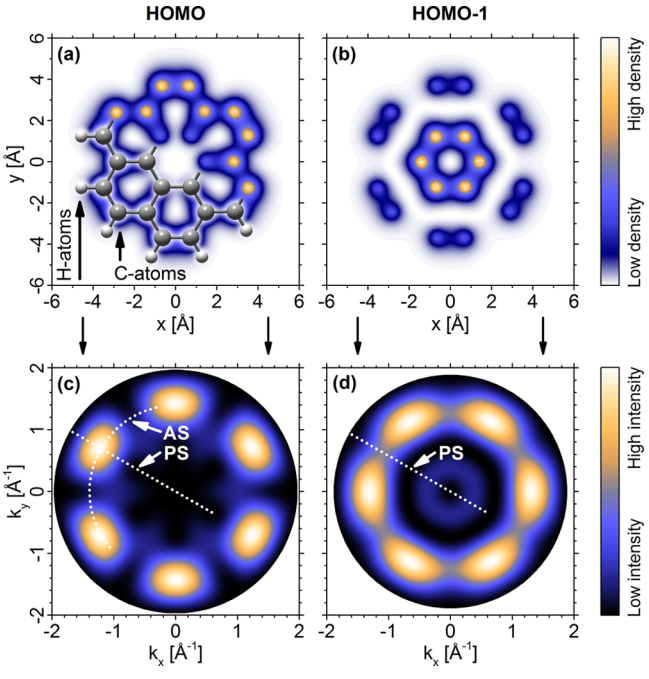

Figure 3. (a,b) z-integrated probability maps of the HOMO and the HOMO−1. (c,d) Simulated momentum maps. Density and intensity scales are adjusted individually. White dotted lines indicate the directions of the azimuthal scans (ASs) and the polar scans (PSs), evaluated in detail in Figure 4.

We now focus on 1D intensity cuts through the momentum maps either in the azimuthal direction or in the polar direction, as indicated by the white dotted lines in Figure 2c,d. These angular scans are compiled in Figure 4, where experimental results and simulations are compared. It is apparent that each measured scan shows a double-peak structure of the main maximum, while the corresponding simulation shows only one. The measured polar scans further exhibit an enhancement of intensity in the $k = -0.50$ Å^{-1} to +0.50 Å^{-1} region, indicating a certain degree of hybridization of the orbitals with the substrate.[2] We remark that the double-peak structure of the angular scans was also observed for different samples measured at room temperature, as can be seen exemplarily in Figure 4a−c (red dotted lines). The decrease in the absolute intensities and the change of the peak height ratio are due to different experimental conditions and are not of major importance for the further discussion. For a more quantitative analysis of the peak features, the curves of the cooled sample were fitted with Gaussian peaks considering a suitable fit range and a constant offset.

One possible explanation for the double-peak appearance of both the experimental AS and PS may be an angular misalignment of the molecule with respect to the substrate's high-symmetry directions. The angles calculated from the peak positions obtained by the fits would lead to a rotational angle in azimuthal direction of 8.4° (using the HOMO AS) and out-of-plane tilt angles of 5.4° (using the HOMO PS) or 8.2° (using the HOMO−1 PS), respectively. However, utilizing the previously mentioned DFT calculations, the molecular orientation is likely not responsible for explaining the double-peak features in the measured polar scans because no tilt of the molecules had been found. It is furthermore apparent that the full widths at half-maximum (FWHM) of the three simulated peaks (Figure 4d−f) are approximately twice as large as the ones of the measurements. The rotational angle calculated from the HOMO AS (8.4°) as well as slightly different rotational angles can thus not cause the peak splitting of the azimuthal scan. Consequently, the properties of isolated coronene molecules are insufficient to explain the measured angular intensity distributions.

Momentum Maps of Free-Standing Coronene Assemblies. Instead of the molecular orientation, the double-peak features in the measured angular scans and thus the substructures in the momentum maps are considered to be caused by a different physical effect, namely, the electronic coupling of 2D aggregated molecules (Figure 5). The influence of the aggregation on the PMM simulations, which is motivated by a redistribution of electron density in the molecular aggregate, shall be separately modeled and discussed in the following. For the simulations presented, we consider a rotational angle of 6°, being obtained by the structural optimization shown in Figure 1c. To account for the film symmetry, six-fold rotational and mirror symmetry were applied

DOI: 10.1021/acs.jpcc.7b03500
J. Phys. Chem. C 2017, 121, 12285−12293

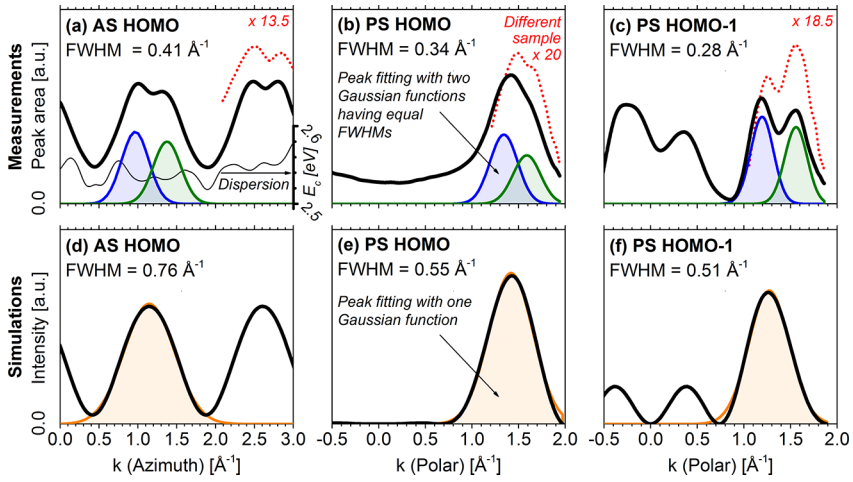

Figure 4. (a,d) Azimuthal scans (AS) of the HOMO. (b,c,e,f) Polar scans (PSs) of the HOMO and the HOMO−1, respectively. Measurements (cf. Figure 2) are shown in the top; simulations (cf. Figure 3) are shown in the bottom row. Angular scans of a different sample measured at room temperature are shown in panels a−c as red dotted lines. The curves are enhanced in intensity with the listed factors to empirically account for different experimental conditions. In panel a also the dispersion extracted from the AS data is shown.

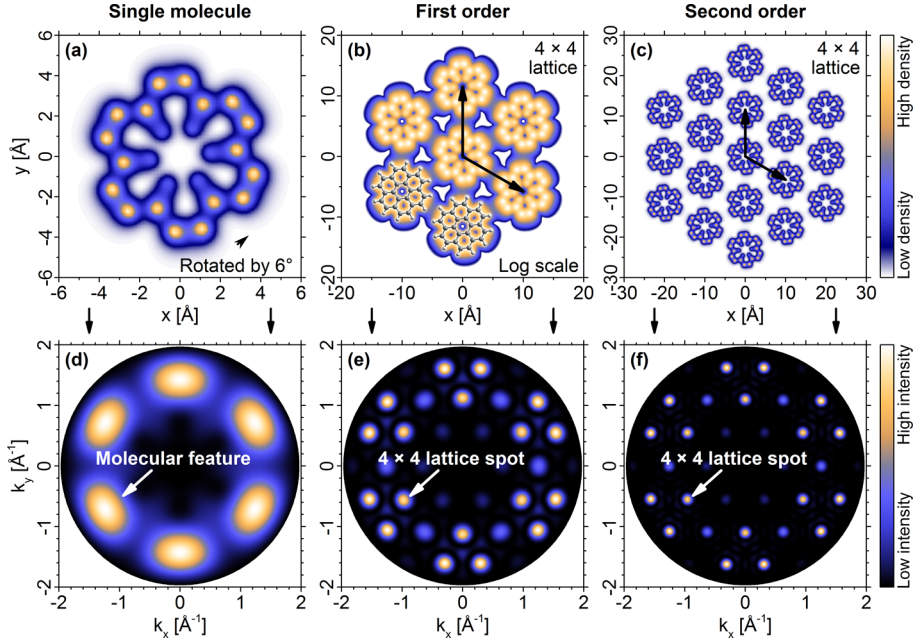

Figure 5. Simulation of the HOMO momentum maps (bottom row) for various assemblies of coronene molecules (top row). The molecules are, in all cases, rotated by 6° around the *z*-axis. In panel b, a logarithmic density scale is chosen to visualize the orbital overlap. Six-fold rotational and mirror symmetries were applied for panels d−f. Density and intensity scales are adjusted individually.

in the PMM simulations of Figure 5 and the ones presented in the following.

First, a coronene molecule surrounded by six other molecules according to the 4 × 4 film lattice is simulated (Figure 5b,e). The momentum map then shows new spots at 4 × 4 reciprocal lattice positions with a FWHM comparable to that of the angular scans. Performing the simulation including the next ring of 12 molecules (Figure 5c,f) further decreases the FWHM of the spots, while their number remains the same. The simulation of the single molecule (Figure 5a,b) confirms that the azimuthal orientation itself is indeed not the origin of the peak splitting because the main maxima are, in contrast with the measurements, featureless.

Besides the assembly of the molecules within the 4 × 4 lattice, also the phase alignment of the molecules' wave functions has to be considered to account for bonding and antibonding coupling.[37] An exemplary antiphase assembly is shown in Figure 6a,c, visualized by numerically summing up $\Psi(x, y, z)$ in the $z > 0$ half space. Moreover, one has to account for the coupling of the two degenerate parts of the HOMO with an exemplary orbital assembly (labeled alternating-phase) shown in Figure 6b,d. While the antiphase assembly was obtained by inverting the phase of certain molecules (marked with the minus signs), the alternating-phase assembly was obtained by mixing the two degenerate parts of the HOMO (labeled P1 and P2). Although the underlying film structure still exhibits in both cases a 4 × 4 geometry in terms of lattice epitaxy, it resembles an 8 × 4 geometry when the phase of the molecular wave function and the degeneracy are regarded as well. Using the antiphase and the alternating-phase assembly

DOI: 10.1021/acs.jpcc.7b03500
J. Phys. Chem. C 2017, 121, 12285−12293

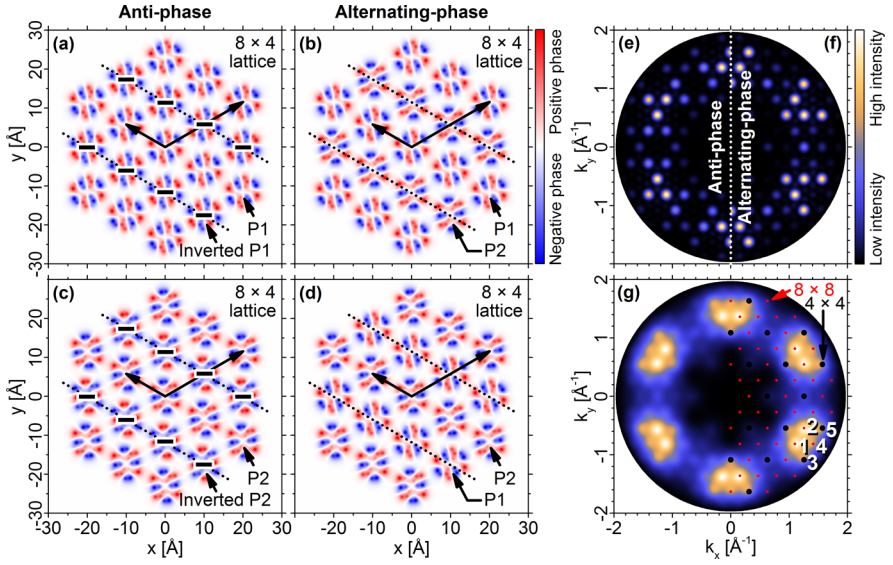

Figure 6. Exemplary antiphase assemblies (a,b) and alternating-phase assemblies (c,d) of the two degenerate HOMO parts P1 and P2. Simulation results are shown in panels e and f, respectively. (g) Final momentum map (see the text for details). Six-fold rotational and mirror symmetries were applied for panels e–g. Phase and intensity scales are adjusted individually.

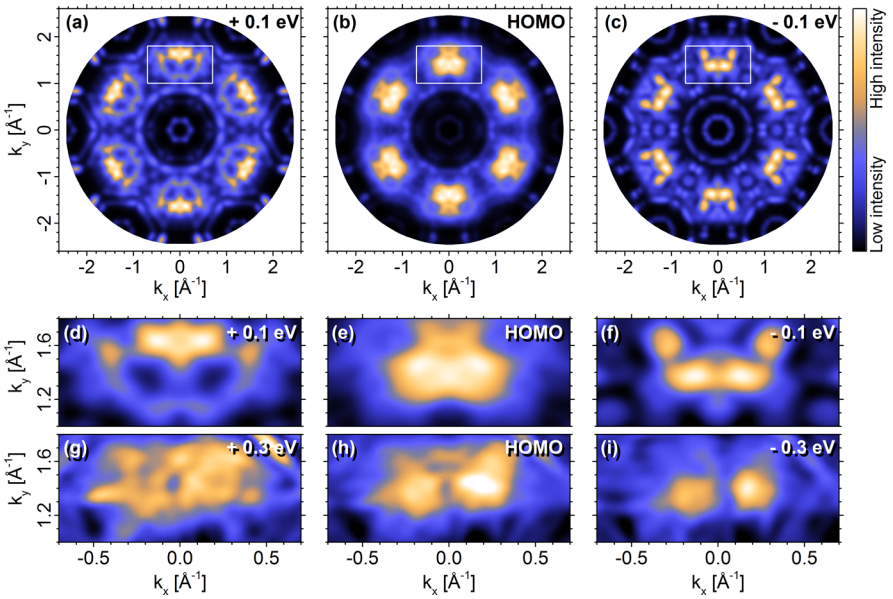

Figure 7. (a–c) Simulated PMMs of the HOMO peak at three different binding energies (E_b(HOMO) + 0.1 eV, E_b(HOMO), and E_b(HOMO) − 0.1 eV). The white rectangles mark the *k*-space regions presented in panels d–f. In comparison, panels g–i show the experimental data at corresponding binding energies. See the text for further details.

for the simulations, spots at 8 × 8 reciprocal lattice positions appear in the momentum maps (Figure 6e,f). In contrast with the PMMs of Figure 6e,f, the momentum map of Figure 5f was calculated on the basis of an in-phase assembly, where spots at the characteristic 8 × 8 positions could not be observed.

Figure 6g shows the momentum pattern using exemplary attenuation factors of f_1 = 0.01 for the first order and f_2 = 0.0001 for the second order of molecules. Here, we introduced f_1 and f_2 as merely empirical factors, which are supposed to account for the orbital coupling between neighboring molecules. Furthermore, the sum of the antiphase, the alternating-phase, and 1/4 of the in-phase alignment was calculated. The attenuation factors as well as the prefactors of the summation are not theoretically founded but were chosen such that the substructure of the measured momentum map is well reproduced (Figure 2c). Note further that from our measurements it cannot be distinguished whether the coupling originates from a direct coupling of the molecules or from a substrate-mediated coupling.[38] In accordance with this, f_1 and f_2 do not assume a specific coupling mechanism.

The five submaxima (labeled by the numbers 1–5 in Figure 6g) compare favorably with the ones observed in the PMM taken at the HOMO energy (Figure 2c). While the subpeaks 3 and 5 can also be explained by an in-phase assembly (4 × 4 geometry), an explanation of the submaxima 1, 2, and 4 requires at least the antiphase or the alternating-phase assembly (8 × 4 or 8 × 8 geometry). A change of the phase alignment with varying *k*-value was also revealed for benzene molecules adsorbed on Ni(111).[37] Both a bonding and an antibonding situation, as expected from ref 37, were observed by us as well

DOI: 10.1021/acs.jpcc.7b03500
J. Phys. Chem. C 2017, 121, 12285–12293

in the ARUPS diagram (Figure 2b). The assignment of bonding and antibonding coupling to dispersion maxima and minima also fits the dispersion map presented in ref 7, where 1 ML coronene films on Au(111) were investigated.

Remaining differences in the relative spot intensities between the experimental and the simulated HOMO PMMs (Figures 2c and 6g) might be due to the specific experimental conditions (cf. black and red dotted lines shown in Figure 4), the fact that also other possible phase alignments than the ones considered here may contribute, and the limitations of the calculation procedure.[39,40] Furthermore, surface effects upon adsorption, such as hybridization and charge transfer,[41,42] as well as the transition of the photoelectron from the sample to the vacuum[15] are not considered in the simulations. However, because the new features in the momentum maps are obviously caused by the molecular arrangement, the double features in the angular scans (Figure 4) as well as the substructure observed in the measured momentum maps (Figure 2c,d) can be interpreted as aggregation properties rather than being caused exclusively by tilt and rotational angles of the molecules.

Momentum Maps of Coronene Monolayers on Ag(111). In the preceding section it was qualitatively shown how molecular assemblies can alter the *k*-space structure and how the phase relations can possibly explain the features in PMMs. The aim of the following section will be to refine the intermolecular phase relations by considering an infinite monolayer rather than a finite-sized cluster of molecules and taking into account the influence of the substrate to compare these simulations to the experimental data.

Our simulations of the PMMs for the coronene/Ag(111) interface are based on the DFT calculations presented above (Figure 1c) using an approach described in previous publications.[6,30] Here, the final state of the photoemission is again assumed to be of plane wave character. Note, however, that we apply an exponential damping of the final state inside the substrate in a direction perpendicular to the surface normal to account for the limited mean-free path of the photoelectrons within the substrate. Relating this ab initio method to the considerations from the previous section, we now sum over all initial states $\psi_{n\vec{k}}$ of Bloch-wave character within the first Brillouin zone instead of summing over only a few contributions with selected phase relations between neighboring molecules. Therefore, the simulations naturally include a possible intermolecular dispersion through the *k*-dependence of the Bloch state energies $\varepsilon_{n\vec{k}}$.

In Figure 7a–c, we show simulated PMMs of the HOMO at three different binding energies centered around the peak maximum. We clearly recognize an energy-dependent variation of the substructure of the main HOMO lobes. To analyze this substructure further, we show a close-up of one of the six equivalent maxima in panels d–f and compare them with the corresponding experimental data in panels g–i. The measured PMMs are taken at three different binding energies, namely at the center of the HOMO emission (h) as well as at a 0.3 eV higher binding energy (g) and a 0.3 eV lower binding energy (i) with respect to the central energy of 2.6 eV. To increase the resolution in the maps, the integration range is decreased to 50 meV. We observe that in both experiment and simulation the intensity center of the main PMM feature moves to smaller k_y-values when the binding energy is decreased. At the same time, an azimuthal splitting (here in k_x-direction) becomes most clear in panels f and i, corresponding to the low binding energy side of the HOMO peak. An overall good agreement between experiment and theory can be inferred from panels d to i of Figure 7. Note that for the simulations a smaller energy spacing of 0.1 eV has been chosen, while a larger energy spread has been chosen for the measured maps due to the experimental broadening in the spectra.

CONCLUSIONS

It was shown that the main features of the (k_x,k_y)-dependent PMMs of 1 ML coronene films on Ag(111) can be described by a photoemission process originating from coupled orbitals of neighboring molecules. The measured PMMs thus carry the signatures of both that of a single molecular orbital and that of the adsorbate lattice. It can be concluded from our calculations that already the inclusion of the nearest and the second-nearest neighbors is sufficient to account for the additional lattice features in the measured momentum maps. We further demonstrate by comparison to PMM simulations that the double-peak features in the angular scans can be explained by neither a tilt nor a rotational angle of the molecules but by the film lattice. PMM simulations performed at a structurally optimized coronene monolayer on Ag(111) confirm the appearance of the substructure due to molecule–molecule and molecule–substrate interactions.

A variety of features caused by the three-fold symmetry of the substrate could be additionally evidenced in the momentum maps. Because a coupling of the orbitals with the substrate is confirmed by means of polar scans, we further conclude that a hybridization between substrate and molecular adsorbate is responsible for the substrate influence on the momentum maps.

AUTHOR INFORMATION

Corresponding Authors

*P.P.: E-mail: peter.puschnig@uni-graz.at.
*T.F.: E-mail: torsten.fritz@uni-jena.de.

ORCID

Roman Forker: 0000-0003-0969-9180
Peter Puschnig: 0000-0002-8057-7795

Present Address

§Institute for Molecular Science, Myodaiji, Okazaki 444-8585, Japan.

Notes

The authors declare no competing financial interest.

ACKNOWLEDGMENTS

This research was partially founded by the DFG (grant nos. FO 770/2-1 and FR 875/16-1). C.U. acknowledges financial support through a Landesgraduiertenstipendium of the State of Thuringia. T.H. and T.K gratefully acknowledge funding from the Studienstiftung des deutschen Volkes and from the Evonik Stiftung, respectively. We further acknowledge financial support from the Austrian Science Fund FWF (P27649-N20). Part of the computational results presented have been achieved using the computing facilities of the University of Graz and the Vienna Scientific Cluster (VSC3).

REFERENCES

(1) Puschnig, P.; Berkebile, S.; Fleming, A. J.; Koller, G.; Emtsev, K.; Seyller, T.; Riley, J. D.; Ambrosch-Draxl, C.; Netzer, F. P.; Ramsey, M. G. Reconstruction of Molecular Orbital Densities from Photoemission Data. *Science* **2009**, *326*, 702–706.

DOI: 10.1021/acs.jpcc.7b03500
J. Phys. Chem. C 2017, 121, 12285–12293

(2) Ziroff, J.; Forster, F.; Schöll, A.; Puschnig, P.; Reinert, F. Hybridization of Organic Molecular Orbitals with Substrate States at Interfaces: PTCDA on Silver. *Phys. Rev. Lett.* **2010**, *104*, 233004.
(3) Stadtmüller, B.; Willenbockel, M.; Reinisch, E. M.; Ules, T.; Bocquet, F. C.; Soubatch, S.; Puschnig, P.; Koller, G.; Ramsey, M. G.; Tautz, F. S.; et al. Orbital tomography for highly symmetric adsorbate systems. *Europhys. Lett.* **2012**, *100*, 26008.
(4) Lüftner, D.; Ules, T.; Reinisch, E. M.; Koller, G.; Soubatch, S.; Tautz, F. S.; Ramsey, M. G.; Puschnig, P. Imaging the wave functions of adsorbed molecules. *Proc. Natl. Acad. Sci. U. S. A.* **2014**, *111*, 605−610.
(5) Puschnig, P.; Boese, A. D.; Willenbockel, M.; Meyer, M.; Lüftner, D.; Reinisch, E. M.; Ules, T.; Koller, G.; Soubatch, S.; Ramsey, M. G.; et al. Energy ordering of molecular orbitals. *J. Phys. Chem. Lett.* **2017**, *8*, 208−213.
(6) Ules, T.; Lüftner, D.; Reinisch, E. M.; Koller, G.; Puschnig, P.; Ramsey, M. G. Orbital tomography of hybridized and dispersing molecular overlayers. *Phys. Rev. B: Condens. Matter Mater. Phys.* **2014**, *90*, 155430.
(7) Graus, M.; Grimm, M.; Metzger, C.; Dauth, M.; Tusche, C.; Kirschner, J.; Kümmel, S.; Schöll, A.; Reinert, F. Electron-Vibration Coupling in Molecular Materials: Assignment of Vibronic Modes from Photoelectron Momentum Mapping. *Phys. Rev. Lett.* **2016**, *116*, 147601.
(8) Kera, S.; Tanaka, S.; Yamane, H.; Yoshimura, D.; Okudaira, K. K.; Seki, K.; Ueno, N. Quantitative analysis of photoelectron angular distribution of single-domain organic monolayer film: NTCDA on GeS(001). *Chem. Phys.* **2006**, *325*, 113−120.
(9) Kubozono, Y.; Mitamura, H.; Lee, X.; He, X.; Yamanari, Y.; Takahashi, Y.; Suzuki, Y.; Kaji, Y.; Eguchi, R.; Akaike, K.; et al. Metal-intercalated aromatic hydrocarbons: a new class of carbon-based superconductors. *Phys. Chem. Chem. Phys.* **2011**, *13*, 16476−16493.
(10) Duhm, S.; Gerlach, A.; Salzmann, I.; Bröker, B.; Johnson, R. L.; Schreiber, F.; Koch, N. PTCDA on Au(111), Ag(111) and Cu(111): Correlation of interface charge transfer to bonding distance. *Org. Electron.* **2008**, *9*, 111−118.
(11) Huempfner, T.; Sojka, F.; Forker, R.; Fritz, T. Growth of coronene on (100)- and (111)-surfaces of fcc-crystals. *Surf. Sci.* **2015**, *639*, 80−88.
(12) Lackinger, M.; Griessl, S.; Heckl, W. M.; Hietschold, M. Coronene on Ag(111) Investigated by LEED and STM in UHV. *J. Phys. Chem. B* **2002**, *106*, 4482−4485.
(13) Musket, R. G.; McLean, W.; Colmenares, C. A.; Makowiecki, D. M.; Siekhaus, W. J. Preparation of atomically clean surfaces of selected elements: A review. *Appl. Surf. Sci.* **1982**, *10*, 143−207.
(14) Damascelli, A. Probing the Electronic Structure of Complex Systems by ARPES. *Phys. Scr.* **2004**, *T109*, 61−74.
(15) Ueno, N.; Kera, S. Electron spectroscopy of functional organic thin films: Deep insights into valence electronic structure in relation to charge transport property. *Prog. Surf. Sci.* **2008**, *83*, 490−557.
(16) Kirchhuebel, T.; Gruenewald, M.; Sojka, F.; Kera, S.; Bussolotti, F.; Ueba, T.; Ueno, N.; Rouillé, G.; Forker, R.; Fritz, T. Self-Assembly of Tetraphenyldibenzoperiflanthene (DBP) Films on Ag(111) in the Monolayer Regime. *Langmuir* **2016**, *32*, 1981−1987.
(17) Frisch, M. J.; Trucks, G. W.; Schlegel, H. B.; Scuseria, G. E.; Robb, M. A.; Cheeseman, J. R.; Scalmani, G.; Barone, V.; Mennucci, B.; Petersson, G. A.; et al. *Gaussian09*, revision E.01; Gaussian Inc.: Wallingford, CT, 2009.
(18) Kresse, G.; Hafner, J. Ab initio molecule dynamics for liquid metals. *Phys. Rev. B: Condens. Matter Mater. Phys.* **1993**, *47*, 558−561.
(19) Kresse, G.; Furthmüller, J. Efficiency of ab-initio total energy calculations for metals and semiconductors using a plane-wave basis set. *Comput. Mater. Sci.* **1996**, *6*, 15−50.
(20) Kresse, G.; Joubert, D. From ultrasoft pseudopotentials to the projector augmented-wave method. *Phys. Rev. B: Condens. Matter Mater. Phys.* **1999**, *59*, 1758−1775.
(21) Neugebauer, J.; Scheffler, M. Adsorbate-substrate and adsorbate-adsorbate interactions of Na and K adlayers on Al(111). *Phys. Rev. B: Condens. Matter Mater. Phys.* **1992**, *46*, 16067−16080.
(22) Perdew, J. P.; Burke, K.; Ernzerhof, M. Generalized Gradient Approximation Made Simple. *Phys. Rev. Lett.* **1996**, *77*, 3865−3868.
(23) Blöchl, P. E. Projector augmented-wave method. *Phys. Rev. B: Condens. Matter Mater. Phys.* **1994**, *50*, 17953−17979.
(24) Monkhorst, H. J.; Pack, J. D. Special points for Brillouin-zone integrations. *Phys. Rev. B: Condens. Matter Mater. Phys.* **1976**, *13*, 5188−5192.
(25) Methfessel, M.; Paxton, A. T. High-precision sampling for Brillouin-zone integration in metals. *Phys. Rev. B: Condens. Matter Mater. Phys.* **1989**, *40*, 3616−3621.
(26) Sony, P.; Puschnig, P.; Nabok, D.; Ambrosch-Draxl, C. Importance of Van Der Waals Interaction for Organic Molecule-Metal Junctions: Adsorption of Thiophene on Cu(110) as a Prototype. *Phys. Rev. Lett.* **2007**, *99*, 176401.
(27) Romaner, L.; Nabok, D.; Puschnig, P.; Zojer, E.; Ambrosch-Draxl, C. Theoretical study of PTCDA adsorbed on the coinage metal surfaces, Ag(111), Au(111) and Cu(111). *New J. Phys.* **2009**, *11*, 053010.
(28) Tkatchenko, A.; Scheffler, M. Accurate Molecular Van Der Waals Interactions from Ground-State Electron Density and Free-Atom Reference Data. *Phys. Rev. Lett.* **2009**, *102*, 073005.
(29) Ruiz, V. G.; Liu, W.; Zojer, E.; Scheffler, M.; Tkatchenko, A. Density-Functional Theory with Screened van der Waals Interactions for the Modeling of Hybrid Inorganic-Organic Systems. *Phys. Rev. Lett.* **2012**, *108*, 146103.
(30) Puschnig, P.; Lüftner, D. Simulation of angle-resolved photoemission spectra by approximating the final state by a plane wave: from graphene to polycyclic aromatic hydrocarbon molecules. *J. Electron Spectrosc. Relat. Phenom.* **2015**, *200*, 193−208.
(31) Yano, M.; Endo, M.; Hasegawa, Y.; Okada, R.; Yamada, Y.; Sasaki, M. Well-ordered monolayers of alkali-doped coronene and picene: Molecular arrangements and electronic structures. *J. Chem. Phys.* **2014**, *141*, 034708.
(32) Hanke, F.; Björk, J. Structure and local reactivity of the Au(111) surface reconstruction. *Phys. Rev. B: Condens. Matter Mater. Phys.* **2013**, *87*, 235422.
(33) Yannoulis, P.; Dudde, R.; Frank, K. H.; Koch, E. E. Orientation of aromatic hydrocarbons on metal surfaces as determined by NEXAFS. *Surf. Sci.* **1987**, *189−190*, 519−528.
(34) Yang, S.-L.; Sobota, J. A.; Howard, C. A.; Pickard, C. J.; Hashimoto, M.; Lu, D. H.; Mo, S.-K.; Kirchmann, P. S.; Shen, Z.-X. Superconducting graphene sheets in CaC_6 enabled by phonon-mediated interband interactions. *Nat. Commun.* **2014**, *5*, 3493.
(35) Wießner, M.; Rodríguez Lastra, N. S.; Ziroff, J.; Forster, F.; Puschnig, P.; Dössel, L.; Müllen, K.; Schöll, A.; Reinert, F. Different views on the electronic structure of nanoscale graphene: aromatic molecule versus quantum dot. *New J. Phys.* **2012**, *14*, 113008.
(36) Kosugi, T.; Miyake, T.; Ishibashi, S.; Arita, R.; Aoki, H. Ab initio electronic structure of solid coronene: Differences from and commonalities to picene. *Phys. Rev. B: Condens. Matter Mater. Phys.* **2011**, *84*, 020507.
(37) Steinrück, H.-P. Angle-resolved photoemission studies of adsorbed hydrocarbons. *J. Phys.: Condens. Matter* **1996**, *8*, 6465−6509.
(38) Wießner, M.; Ziroff, J.; Forster, F.; Arita, M.; Shimada, K.; Puschnig, P.; Schöll, A.; Reinert, F. Substrate-mediated band-dispersion of adsorbate molecular states. *Nat. Commun.* **2013**, *4*, 1514.
(39) Weiß, S.; Lüftner, D.; Ules, T.; Reinisch, E. M.; Kaser, H.; Gottwald, A.; Richter, M.; Soubatch, S.; Koller, G.; Ramsey, M. G.; et al. Exploring three-dimensional orbital imaging with energy-dependent photoemission tomography. *Nat. Commun.* **2015**, *6*, 8287.
(40) Dauth, M.; Wiessner, M.; Feyer, V.; Schöll, A.; Puschnig, P.; Reinert, F.; Kümmel, S. Angle resolved photoemission from organic semiconductors: orbital imaging beyond the molecular orbital interpretation. *New J. Phys.* **2014**, *16*, 103005.
(41) Forker, R.; Gruenewald, M.; Fritz, T. Optical differential reflectance spectroscopy on thin molecular films. *Annu. Rep. Prog. Chem., Sect. C: Phys. Chem.* **2012**, *108*, 34−68.

DOI: 10.1021/acs.jpcc.7b03500
J. Phys. Chem. C 2017, 121, 12285−12293

(42) Forker, R.; Fritz, T. Optical differential reflectance spectroscopy of ultrathin epitaxial organic films. *Phys. Chem. Chem. Phys.* **2009**, *11*, 2142−2155.

DOI: 10.1021/acs.jpcc.7b03500
J. Phys. Chem. C 2017, 121, 12285−12293